Multitemporal Fluctuations in L-Band Backscatter From a Japanese Forest

Manabu Watanabe, *Senior Member, IEEE*, Takeshi Motohka, Tomohiro Shiraishi, Rajesh Bahadur Thapa, Chinatsu Yonezawa, *Member, IEEE*, Kazuki Nakamura, *Member, IEEE*, and Masanobu Shimada, *Fellow, IEEE*

***Abstract*—The temporal variations (diurnal and annual) in arboreal ($\varepsilon_{\mathrm{Tree}}$) and bare soil ($\varepsilon_{\mathrm{Soil}}$) dielectric constants and their correlation with precipitation were examined for several trees in Japan. A significant (1 σ (standard deviation) and 2 σ) $\varepsilon_{\mathrm{Tree}}$ increase is observed after rainfall at 89.8% and 90.5% probability. However, rainfall does not always induce significant $\varepsilon_{\mathrm{Tree}}$ increases. Rainfall of more than 5 mm/day can induce 1 σ $\varepsilon_{\mathrm{Tree}}$ Tree increase at a 59.6% probability. In order to examine whether the increase in $\varepsilon_{\mathrm{Tree}}$ affects the L-band σ^0 variation in a forest, the four-year temporal variation of the L-band backscattering coefficient (σ^0) was estimated from observations by the Advanced Land Observing Satellite Phased Array type L-band Synthetic Aperture Radar. Observed maximum absolute deviations from the mean over the forest area were 1.0 and 1.2 dB for σ^0_{HH} and σ^0_{HV}, respectively, and 4.0 and 3.0 dB over open land. σ^0 and rainfall correlations show that $\varepsilon_{\mathrm{Tree}}$ and $\sigma^0_{\mathrm{Forest}}$ are proportional to precipitation integrated over seven or eight days; $\varepsilon_{\mathrm{Soil}}$ and $\sigma^0_{\mathrm{Open\ land}}$ are proportional to precipitation integrated over three days. This finding indicates that $\varepsilon_{\mathrm{Tree}}$ variations influence $\sigma^0_{\mathrm{Forest\ areas}}$. A stronger correlation between σ^0_{HV} and precipitation is observed in several sites with low σ^0_{HV}, where less biomass is expected, and several sites with high σ^0_{HV}, where more biomass is expected. A weaker correlation between σ^0_{HV} and precipitation is observed for several sites with high σ^0_{HV}. These differences may be explained by the different contributions of double bounce scattering and potential transpiration, which is a measure of the ability of the atmosphere to remove water from the surface through the processes of transpiration. The two other results were as follows: 1) The functional relation between aboveground biomass and σ^0 showed dependence on precipitation data, this being an effect connected with seasonal changes of the $\varepsilon_{\mathrm{Tree}}$. This experiment reinforces the fact that the dry season is preferable for retrieval of woody biomass from inversion of the functional dependence of SAR backscatter and for avoiding the influence of rainfall. 2) The complex dielectric constant for a tree trunk, which is measured between 0.2 and 6 GHz, indicates that free water is dominant in the measured tree.**

***Index Terms*—Biomass, dielectric constant, forest, Phased Array type L-band Synthetic Aperture Radar (PALSAR), temporal variation.**

I. Introduction

THE aboveground biomass (AGB) for a low-biomass area (i.e., for a biomass of less than 100 tons/ha) is expected to be derived from the radar backscattering coefficient (σ^0) in the L-band [1]–[3]. The highest correlation between biomass and σ^0_{HV} is around 0.8 [2], which is a value that is considered insufficient for practical use, depending upon the application and the use of the data.

Two possible causes for the degradation in the correlation are as follows: 1) The relationship depends on the forest structure [2], [3], where differences in σ^0-AGB have been observed between forests, woodlands, open woodlands, and alignment of tree plantation. 2) The temporal variation of σ^0, three types of which, due to rainfall, diurnal change, and freeze/snow cover in a forest area, have been reported.

Enhanced L-band backscatter following rainfall events was reported by Lucas *et al.* [3]. Steele-Dunne *et al.* [4] demonstrated the differences between the C-band wind scatterometer measurements from the morning (descending) and evening (ascending) passes of the European Remote Sensing (ERS) 1/2 satellite. They pointed out that these differences correspond to the onset of vegetation water stress. Decreases in σ^0 due to the freezing of the soil and vegetation or snow cover are reported in the L- and C-band over forest areas during winter [5], [6].

Variations in the tree dielectric constant ($\varepsilon_{\mathrm{Tree}}$), which may induce variations in σ^0, have been investigated. Several ground measurements of the tree dielectric constant have been obtained. McDonald *et al.* [7], [8] used time-domain reflectometry (TDR) and examined the relationship between the xylem tissue dielectric constant, xylem sap flux density, and xylem sap chemical composition as measured in the stems of two Norway spruce trees in the Fichtelgebirge region of Northern Bavaria, Germany. The xylem sap flux and ε at several heights along the tree trunks were continuously monitored from June to October in 1995. The study showed a diurnal variation in $\varepsilon_{\mathrm{Tree}}$. Salas *et al.* [9] investigated the diurnal changes in the dielectric properties of trunk wood with C-, L-, and P-band dielectric probes. These properties were found to correlate with diurnal fluctuations in water potential.

However, few studies have monitored the variations of $\varepsilon_{\mathrm{Tree\&Soil}}$ and $\sigma^0_{\mathrm{Forest\&Open\ land}}$ and have attempted to correlate the two parameters in the same geographical location. In this paper, the following experimental analyses were

Manuscript received March 7, 2014; revised October 18, 2014 and December 26, 2014; accepted March 11, 2015. This work was supported by the Japan Society for the Promotion of Science Grants-in-Aid for Scientific Research, specifically (B) 22404001 and (C) 21510004.

M. Watanabe, T. Motohka, T. Shiraishi, R. B. Thapa, and M. Shimada are with the Japan Aerospace Exploration Agency/Earth Observation Research Center, Ibaraki 305-8505, Japan (e-mail: watanabe.manabu@jaxa.jp; motooka.takeshi@jaxa.jp; shiraishi.tomohiro@jaxa.jp; rajesh.thapa@jaxa.jp; shimada.masanobu@jaxa.jp).

C. Yonezawa is with the Graduate School of Agricultural Science, Tohoku University, Miyagi 981-8555, Japan (e-mail: chinatsu@bios.tohoku.ac.jp).

K. Nakamura is with The National Institute of Advanced Industrial Science and Technology, Ibaraki 305-8568, Japan (e-mail: nakamura-kazuki@aist.go.jp).

Color versions of one or more of the figures in this paper are available online at http://ieeexplore.ieee.org.

Digital Object Identifier 10.1109/TGRS.2015.2415832

TABLE I
SUMMARY OF TDR MEASUREMENTS FOR TREE TRUNKS

Place	Tomakomai			Tsukuba	
Experiment ID	TOMAKOMAI1	TOMAKOMAI2	TOMAKOMAI3	TSUKUBA	
Tree ID	PICEA1_TOM	PICEA2_TOM	ABIES_TOM	JRP1_TSU	JRP2_TSU
DBH *(cm)	33.7	27.4	26.4	40.0	42.3
Name of tree (*Nomenclature*)	PICEA (*Picea glehnii Masters*)		ABIES (*Abies sachalinensis*)	Japanese red pine (*Pinus densiflora Sieb. et Zucc)*	
Planted year	1960		1963	Unknown	
Term of experiment	May 1 - June 6, 2011	June 8 - September 16, 2011	September 1 - October 11, 2012	September 1 - October 30, 2011	
Measured height	2 m	2 m	1.5 and 6.4 m	2 m	

* Diameter at breast height

performed: 1) temporal variation (diurnal, yearly) of $\varepsilon_{\mathrm{Tree}}$ and $\varepsilon_{\mathrm{Soil}}$ and their correlations with precipitation data; 2) correlation between σ^0 and precipitation data; and 3) relation between σ^0 and AGB and its dependence on precipitation. Based on these analyses, the relationships between $\sigma^0_{\mathrm{Forest\ area\&Open\ land}}$, $\varepsilon_{\mathrm{Tree\&Soil}}$, and precipitation are discussed.

II. EXPERIMENT AND DATA ANALYSIS

A. Biomass Data Collection in Tomakomai

Field biomass measurements were performed from 2005 to 2012 in the Tomakomai National Forest, located at longitude E 141° and latitude N 42° 44′. Volcanogenous regosol, obtained from the Mt. Tarumae eruption, is the main component of the soil in this area. Minimal litter and understory vegetation appear in this area because of the frequent cutting of the undergrowth and thinning. Many 500 × 500 m stands are distributed and often subdivided into several substands. One or two even-aged forest species are planted in stands or substands. Biomass measurements were carried out in 32 areas. Four major species were found: Akaezo-matsu (Japanese, Nomenclature: *Picea glehnii Masters*, hereafter referred to as PICEA), Todomatsu (Japanese, Nomenclature: *Abies sachalinensis*, hereafter ABIES), Karamatu (Japanese, Nomenclature: *Larix kaempferi*, hereafter larch), and Ezo-matsu (Nomenclature: *Picea jezoensis* Carr, hereafter PICEAJ).

One biomass measurement area consisted of a 20 m × 20 m subarea in a stand. Tree heights and diameters at breast height (DBH) were measured for all trees in the subarea. A smaller 10 m × 10 m subarea was designated within the larger subarea if many small trees were found. Only small trees with a diameter less than a specific criterion (typically 5–10 cm) were measured in the 10 m × 10m subarea, whereas the rest of the trees were measured in the 20 m × 20 m subarea. The trunk volume, i.e., V (m^3), was calculated for each tree from the tree height, i.e., H (m), and the DBH (cm). The volume formulas derived in the Tomakomai area [10], which includes our test areas, were used in this process. The derived trunk volumes were converted to aboveground volumes using a constant-expansion factor of 1.36, which is defined as the ratio of AGB to the trunk biomass, and represents the ratio of crown-to-trunk biomass. Finally, the aboveground volumes were converted into AGB using the dry-matter density, e.g., 0.391 g/cm^3 for PICEA, 0.314 g/cm^3 for PICEAJ, 0.329 g/cm^3 for ABIES, and 0.444 g/cm^3 for larch [11]. Unlike natural or secondary forests, the test site in this study is a well-managed national forest with a flat topography. Several field measurements were carried out within a stand at different locations to check the inhomogeneity of the biomass within the site. The results showed that the inhomogeneity was 4.2%–17.9%.

B. TDR and FDR Measurements of the Dielectric Properties of the Tree Trunk and Soil

Both TDR and FDR (frequency-domain reflectometry) instruments are devices used to directly measure the real part of ε. The TDR and FDR devices that were used have low temperature sensitivity. Temperature-induced drift is ±0.3% for the TDR and negligible for the FDR. The ε was measured on an hourly basis. The values were recorded in a data logger. The soil moisture was recorded in a similar fashion as the Tomakomai experiment. A summary of the experiment is summarized in Table I, and the image of the site of the TOMAKOMAI2 experiment is presented in Fig. 1.

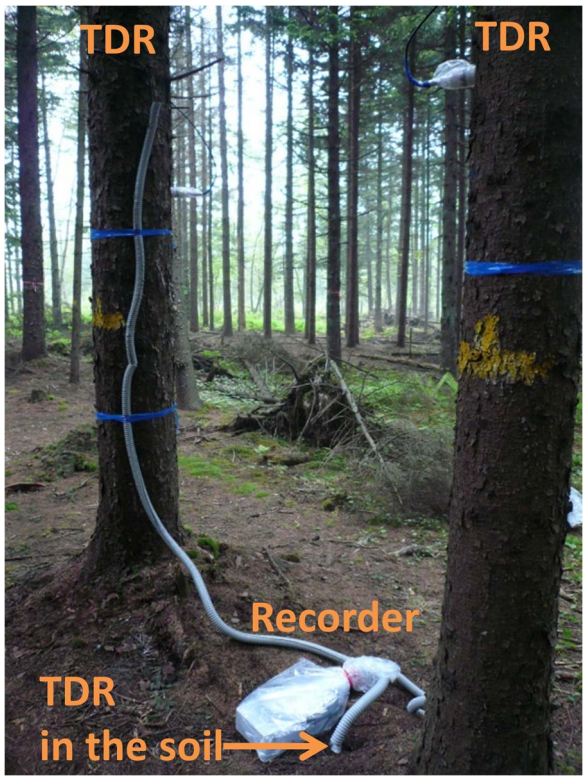

Fig. 1. TOMAKOMAI2 experiment site photograph.

Weather data were also obtained from a station of the Japan Meteorological Agency, which is located around 4 km away from the Tomakomai test sites. Weather data were also obtained from the Japan Meteorological Agency, which is located ∼1 km from the Tsukuba test site. Hourly mean precipitation, air temperature, relative humidity, and sunshine duration recorded at the weather stations were used to establish a relationship with the ε increase.

C. PALSAR Data Analysis in Tomakomai

Ten Phased Array type L-band Synthetic Aperture Radar (PALSAR) observations were made over the Tomakomai National Forest, except during winter, when decreases in σ^0 due to the freezing of the soil and vegetation or snow cover are reported [5], [6]. The off-nadir angle is 34.3°, the path number is 400, polarizations are HH (horizontal transmitting/horizontal receiving) and HV (horizontal transmitting/vertical receiving), and the flight direction is ascending for the observations. The observation dates are presented in Table II. One of the PALSAR images taken on August 18, 2007 is presented in Fig. 2. Because a typhoon hit in September 2004, most of the trees in some sites had fallen down. The fallen trees were removed, and replanting started in 2005. These open land areas with very young trees are indicated in yellow in Fig. 2.

Both orthorectification and level 1.1 data were processed by PolSARpro software [12] to produce a 4-look image. Radiometric calibration was performed on the basis of the following equation:

$$\sigma^0[\mathrm{dB}] = 10\log_{10}\left|I_1^2 + Q_i^2\right| + CF - 32.0 \qquad (1)$$

TABLE II
OBSERVATION DATE FOR PALSAR DATA USED IN THE ANALYSIS AND INTEGRATED PRECIPITATION FOR ZERO TO SEVEN DAYS BEFORE THE PALSAR OBSERVATION. OBSERVATION TIME FOR PALSAR IS 21:59 (JST)

Observation Date	Precipitation							
	1 hour	1 day	2 day	3 day	4 day	5 day	6 day	7 day
August 18, 2007	0	0	5.5	18	18	18	18	18
October 3, 2007	0	0	0	0	0	0	17	22.5
May 20, 2008	2	55	55	55	55	55	55	61.5
July 5, 2008	0	0	4.5	9	9	9	9	9
October 5, 2008	0	0	6	6.5	6.5	9.5	9.5	9.5
July 8, 2009	0	55	55	55	55.5	55.5	55.5	55.5
August 23, 2009	0	0.5	0.5	19.5	31.5	41.5	42	43
October 8, 2009	5	32.5	32.5	32.5	32.5	40	40	71
July 11, 2010	0	0	2	2.5	7	7	7	7
October 11, 2010	0	0	31.5	34.5	34.5	34.5	34.5	34.5

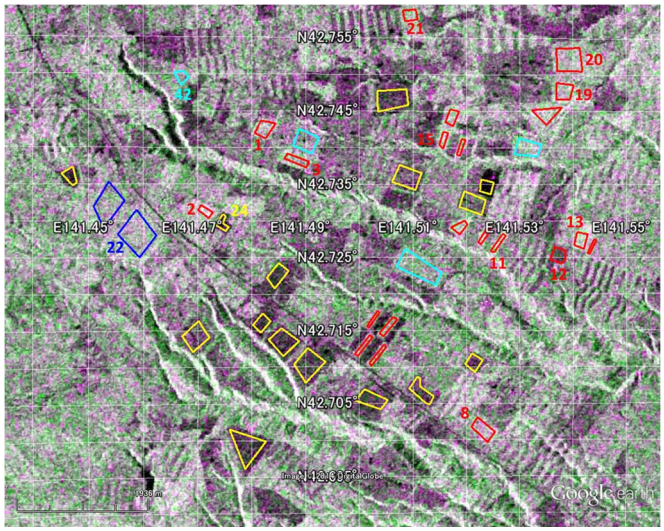

Fig. 2. PALSAR image acquired on August 18, 2007 (R : G : B = HH : HV : HH). Analysis areas are overlaid on the image. Red: PICEA; Cyan: ABIES; Blue: Larch; Yellow: vacant piece of land/area with very young planted trees. Site numbers from the paper are presented.

where σ^0 is the backscattering coefficient, I and Q are the digital numbers of each complex number pixel, and CF is the calibration factor of −83.0 [13]. Speckle filtering has not been applied to the data, because 140–3740 looks/area were averaged to derive the digital number for each test site, reducing speckle noise. The error for each area was a maximum of 0.2 dB. The results were the same, and the results derived from the data processed by PolSARPro are presented in this paper.

Ten sets of PALSAR data were used to examine the variation in σ^0 over four years. In total, 42 areas within a scene were selected (see Fig. 2) for examining variations in σ^0 over the study period. Large and homogeneous areas with a single species were selected for the forest stands. Among the 42 selected areas, 21 areas were occupied by PICEA, four were occupied by ABIES, two were occupied by larch, and 15 sites were open land or newly planted trees. In open land and newly planted

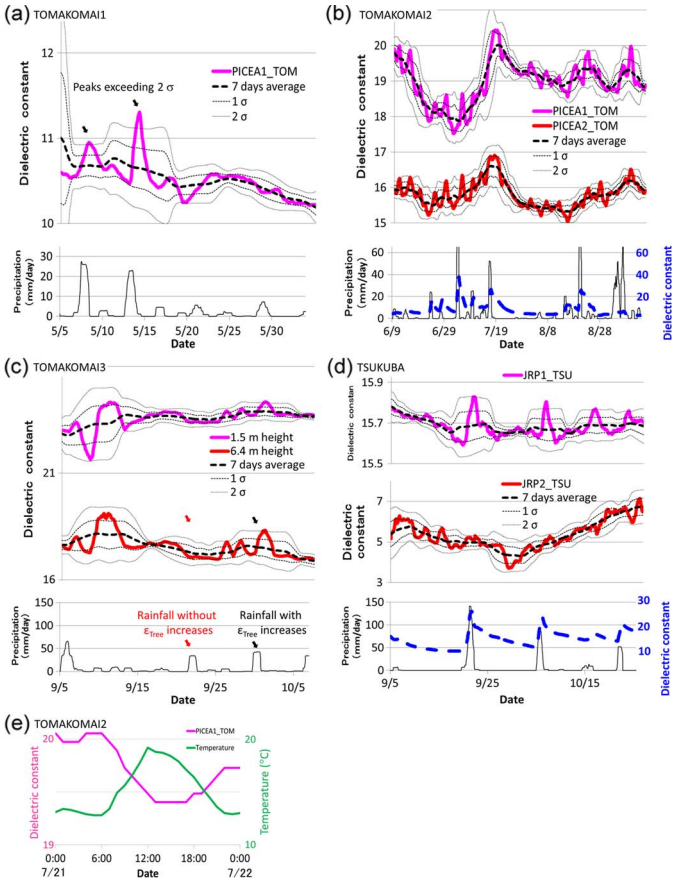

Fig. 3. 24-h averaged variation of ε and precipitation over time for the (a) TOMAKOMAI1 experiment, the (b) TOMAKOMAI2 experiment, the (c) TOMAKOMAI3 experiment, and the (d) TSUKUBA experiment. (e) Variation of ε and temperature recorded by TDR without 24-h average. The dashed line is the seven-day averaged data, and the bold/thin dotted lines indicate the standard deviations (1 and 2 σ).

tree areas, new planting was carried out in 2005 or later, or not planted as of 2010. Since apparent differences were not observed between the open land and newly planted tree areas, this category was regarded as one. Temporal variations in σ^0_{HH} and σ^0_{HV} were examined for all sites.

Weather data were obtained from the Japan Meteorological Agency. Weather measurement stations are located ~13 km from the Tomakomai test sites.

III. Results

A. Relationship Between $\varepsilon_{\mathrm{Tree}}/\varepsilon_{\mathrm{Soil}}$ and Precipitation

The temporal variation in the real part of ε derived from TDR and FDR measurement and precipitation are plotted in Fig. 3. The 24-h averaged ε is plotted to remove the diurnal change, and the precipitation data are also averaged over 24 h for comparison with ε [see Fig. 3(a)–(d)]. Two large peaks exceeding 2 σ (standard deviation), indicated by black arrows in Fig. 3(a), are observed for the $\varepsilon_{\mathrm{Tree}}$ curve in the TOMAKOMAI1 experiment. The peaks nearly coincide with the peaks in the precipitation values. $\varepsilon_{\mathrm{Tree}}$ exceeds the 1 σ line 28 h after rain began.

The other peak observed in the TOMAKOMAI1 experiment shows a similar time delay between precipitation and $\varepsilon_{\mathrm{Tree}}$ exceeding 1 σ.

TABLE III
Number of $\varepsilon_{\mathrm{Tree}}$ Increase Events Connected With Rainfall

Experiment ID	Tree ID		Number of events: Advanced rainfall within 2 day	Number of events: $\varepsilon_{\mathrm{Tree}}$ exceeding more than 2 σ	Number of events: Advanced rainfall within 2 day	Number of events: $\varepsilon_{\mathrm{Tree}}$ exceeding more than 1 σ
Tomakomai 1	PICEA1_TOM		2	2	2	2
Tomakomai 2	PICEA1_TOM		3	3	12	12
	PICEA2_TOM		8	8	14	14
Tomakomai 3	ABIES_TOM	1.5m height	1	1	4	4
		6.4m height	1	1	4	4
Tsukuba	JRP1_TSU		4	5	5	7
	JRP2_TSU		0	1	3	6
Total			19	21	44	49
Rate (%)				90.5		89.8

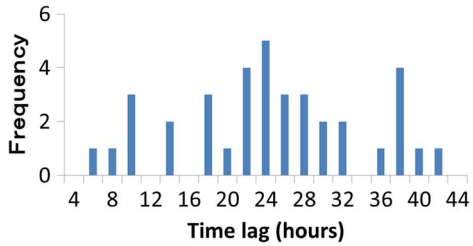

Fig. 4. Histogram of the time lag between $\varepsilon_{\mathrm{Tree}}$ exceeding 1 σ and start of rainfall.

The $\varepsilon_{\mathrm{Tree}}$ increase connected with the advanced rainfall event was also observed in the TOMAKOMAI2/3 experiment and JRP1_TSU of the Tsukuba experiment. The temporal variations in $\varepsilon_{\mathrm{Tree}}$ recorded at 1.5- and 6.4-m tree height are very similar [see Fig. 3(c)]. Very small, but significant, $\varepsilon_{\mathrm{Tree}}$ increases of 0.1–0.2 are observed for JRP1_TSU in TSUKUBA [see Fig. 3(d)].

The number of $\varepsilon_{\mathrm{Tree}}$ increase events connected with the advanced rainfall events was examined (see Table III). A histogram of the time lag between the $\varepsilon_{\mathrm{Tree}}$ exceeding 1 σ and the start of the rainfall is presented in Fig. 4. The 24-h averaged $\varepsilon_{\mathrm{Tree}}$ values exceeding 1 and 2 σ are found when advanced rainfall events occur with 89.8% and 90.5% probability. No clear relationship between 24-h averaged $\varepsilon_{\mathrm{Tree}}$ increase events and other weather parameters such as air temperature, relative humidity, and sunshine duration were observed.

Advanced rainfall events do not always induce significant $\varepsilon_{\mathrm{Tree}}$ increases. For example, rainfall on September 21 did not induce $\varepsilon_{\mathrm{Tree}}$ increases [red arrow in Fig. 3(c)], whereas rainfall on September 28 induced $\varepsilon_{\mathrm{Tree}}$ increases exceeding 2 σ [black arrow in Fig. 3(c)]. The number of rainfall events with more than 5 mm/day connected with $\varepsilon_{\mathrm{Tree}}$ increases of more than 1 σ is examined, and the probability was determined as 59.6%.

Hourly temporal variations in $\varepsilon_{\mathrm{Tree}}$ (without 24-h averaging) for TOMAKOMAI2 are presented in Fig. 3(e), with temperatures recorded by TDR. Diurnal changes are observed here, and almost all the data show diurnal change. The maximum diurnal change is observed on September 5 in TSUKUBA, and the variation of $\varepsilon_{\mathrm{Tree}}$ is 5.3 (from 4.4 to 9.7). This large variation is indicative of the rainfall in early September. The

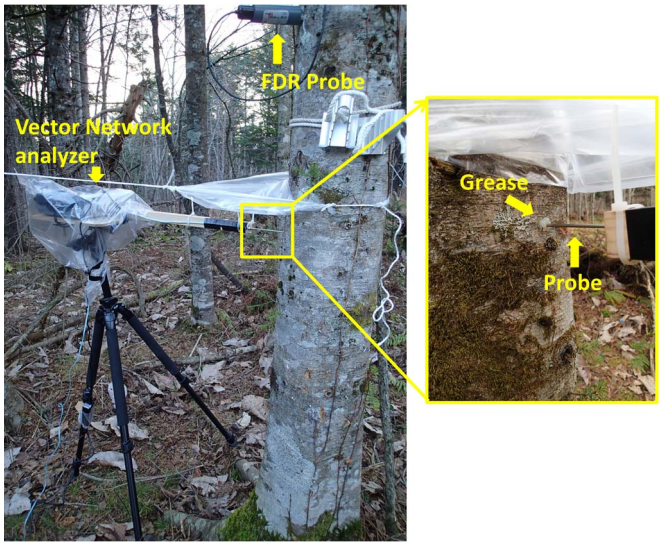

Fig. 5. Photograph of the system used to measure the complex dielectric constant of a tree trunk in site 42 of the Tomakomai Forest.

diurnal variation of $\varepsilon_{\mathrm{Tree}}$ is usually less than 1. The peaks of $\varepsilon_{\mathrm{Trees}}$ occur in the morning (6:00 A.M.–9:00 A.M.), and the lowest points are seen in the evening (16:00 P.M.–18:00 P.M.). This is different from temperature [see Fig. 3(e)], where highs emerge around noon and lows emerge around midnight. This fact also indicates that only minor moisture variations are caused artificially by temperature fluctuations.

B. Imaginary Part of ε for Tree Trunks

To examine the effect of the imaginary part of $\varepsilon_{\mathrm{Tree}}$ for trunks, an additional experiment was performed in site 42 of the Tomakomai Forest. The open-ended coaxial probe technique [14] is adapted to measure temporal variations of complex dielectric constants. The system consists of an SMA coaxial cable connected to a dielectric probe and a vector network analyzer.

The complex dielectric constant ranges from 200 MHz to 6 GHz. The probe system is calibrated by measuring the complex reflection coefficient under three terminal conditions: 1) open circuit; 2) short circuit; and 3) probe immersed in acetone. A photo of the system is presented in Fig. 5.

The bark of the tree is removed, and the probe is carefully adhered to the surface of the tree to ensure that no air gaps remain. Grease is put on the scar and around the probe to prevent drying, and the results are not affected. The device is carefully covered with vinyl, so that the grease and probe are shielded from rainfall.

The surface temperature of the tree trunk is measured via a radiation thermometer and is used to correct the temperature dependence of the dielectric constant. The temporal variation in the real part of $\varepsilon_{\mathrm{Tree}}$ is simultaneously recorded by FDRs. The experiment was conducted from 11:00 on November 16 to 7:00 on November 18, 2012. There was rain during the experiment, starting from 3:00 to 23:00 on November 17.

The results are shown in Fig. 6(a). The $\varepsilon_{\mathrm{Tree}}$ measured using the open-ended coaxial probe technique is 18.4–2.5 i at 1.27 GHz as of 15:00 of November 16. McDonald *et al.* [7], [8]

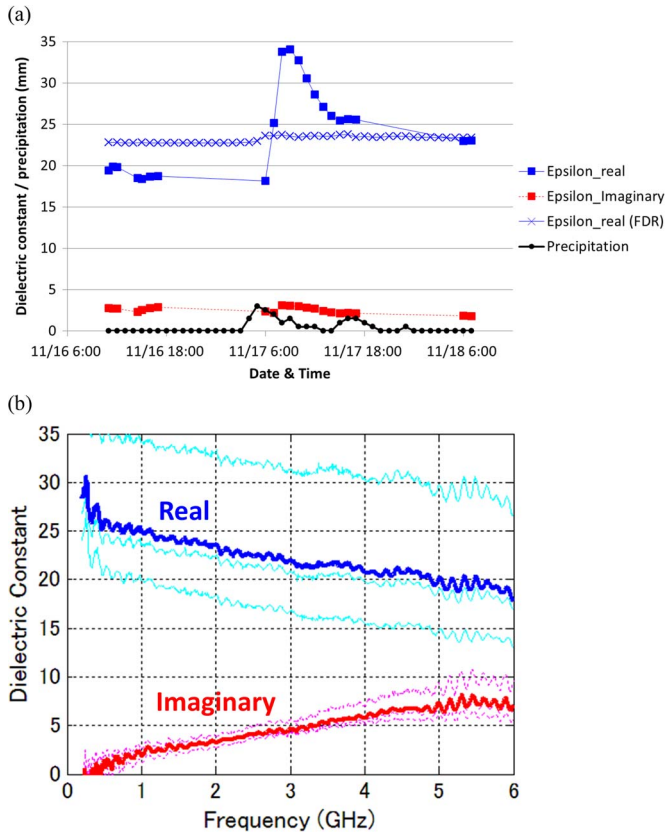

Fig. 6. (a) Temporal variation of the complex dielectric constant of a tree (ABIES_TOM) was measured by an open-ended coaxial probe technique. Real part of dielectric constant measured by FDR is also plotted. (b) Frequency dependence of complex dielectric constant for a tree trunk. Solid blue line, $\varepsilon_{\mathrm{Real}}$ average; solid red line, $\varepsilon_{\mathrm{Imaginary}}$ average; light blue/cyan, three of each measurement.

reported that the imaginary part of ε was 0–3 for the P-band. This result is similar to our experiment. The difference in the real part of $\varepsilon_{\mathrm{Tree}}$ derived by the coaxial probe technique and FDR comes from the difference between the measured depth from the tree surface and the frequency measured. The dielectric constant recorded by the coaxial probe technique and FDR start to increase around 5:00 to 6:00, that is, 2–3 h after the rain starts. However, the change in $\varepsilon_{\mathrm{Tree}}$ is remarkable for the real part. This implies that the real part is the main factor affecting to represent the radar backscattering conditions of a forest.

The frequency dependence of a complex dielectric constant of a tree trunk measured during the experiment is presented in Fig. 6(b). The real part of ε is monotonically decreasing, whereas the imaginary part is increasing. Details are discussed in Section IV-D.

C. Temporal Variation of σ^0

To examine how $\varepsilon_{\mathrm{Tree}}$ increases affect L-band σ^0 variations in a forest; the four-year temporal variation of σ^0_{HH} and σ^0_{HV} over the forest area is investigated. The lowest returns in HH and HV polarizations observed are -14.4 and -23.0 dB, respectively. The noise equivalent σ^0 for dual polarization with the 34.3 off-nadir angle is -32 and -34 dB [13], respectively. All observed signals were higher than the noise level.

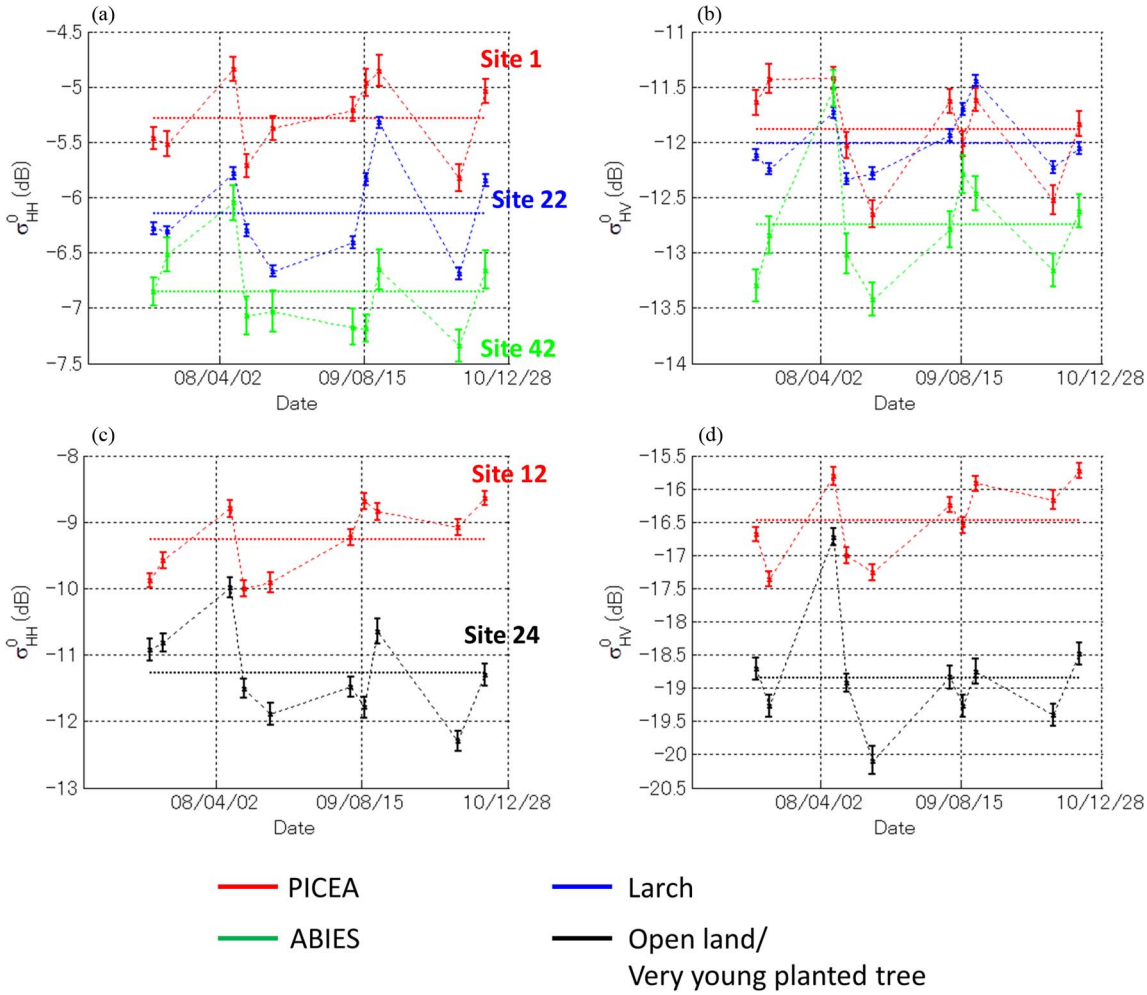

Fig. 7. Four-year temporal variation of σ^0_{HH} and σ^0_{HV} over the forest area. Five representative regions were selected and plotted for σ^0_{HH} in (a) and (c) and for σ^0_{HV} in (b) and (d), respectively, where error bars (standard error of digital number in an area) and average (dotted lines) were added.

Five representative sites were selected, and four-year temporal variations of σ^0_{HH} and σ^0_{HV} are plotted in Fig. 7. Error bars and average lines are superimposed in the figure. The maximum deviation from the mean ranges from 0.4 to 1.2 dB for PICEA in HV polarization. Site 1 (one of five representative regions) shows the maximum deviation of 0.8, which is the medium value of the range.

The maximum deviation from the mean in HV polarization ranges from 1 to 3 dB for open land. Site 24 (one of five representative regions) shows the maximum deviation of 2.1, which is the medium value of the range. The same forest stands were selected in the HH case to compare with the HV case, and almost the same variation pattern was observed. Site 12 of the five representative regions shows the lowest σ^0, because the site is a young forest stand where the AGB is 15.9 tons/ha as of August 2010.

Statistical properties of five selected sites are presented in Table IV. Maximum deviations from the mean of 1.0 and 1.2 dB are observed in HH and HV polarizations, respectively, over the forested areas, and maximum deviations from the mean of 4.0 and 3.0 dB, respectively, are observed over open land.

Radiometric accuracy of the PALSAR is 0.76 dB, which is estimated from corner reflectors (CRs), and 0.17 dB, which is estimated from Sweden CRs 5 m in size (the biggest CR used for the PALSAR calibration) [13]. These values are lower than 1 dB; and the temporal variation is significant. The maximum deviations of 4.0 and 3.0 dB were observed on May 20, 2008. A

TABLE IV
STATISTICAL PROPERTIES OF FIVE SELECTED SITES SHOWN IN FIG. 7

	Site		1	12	22	24	42
	Tree species		PICEA	PICEA	PICEA	PICEA	PICEA
σ^0_{HH} (dB)	Average		-5.3	-9.3	-6.1	-11.3	-6.9
	Deviation from the mean	Minimum	0.1	0.0	0.1	0.0	0.0
		Maximum	0.5	0.7	0.8	1.3	0.8
	Error (average)		0.1	0.1	0.1	0.2	0.2
σ^0_{HV} (dB)	Average		-11.9	-16.5	-12.0	-18.8	-12.7
	Deviation from the mean	Minimum	0.0	0.1	0.0	0.0	0.1
		Maximum	0.8	0.9	0.6	2.1	1.2
	Error (average)		0.1	0.1	0.1	0.2	0.2

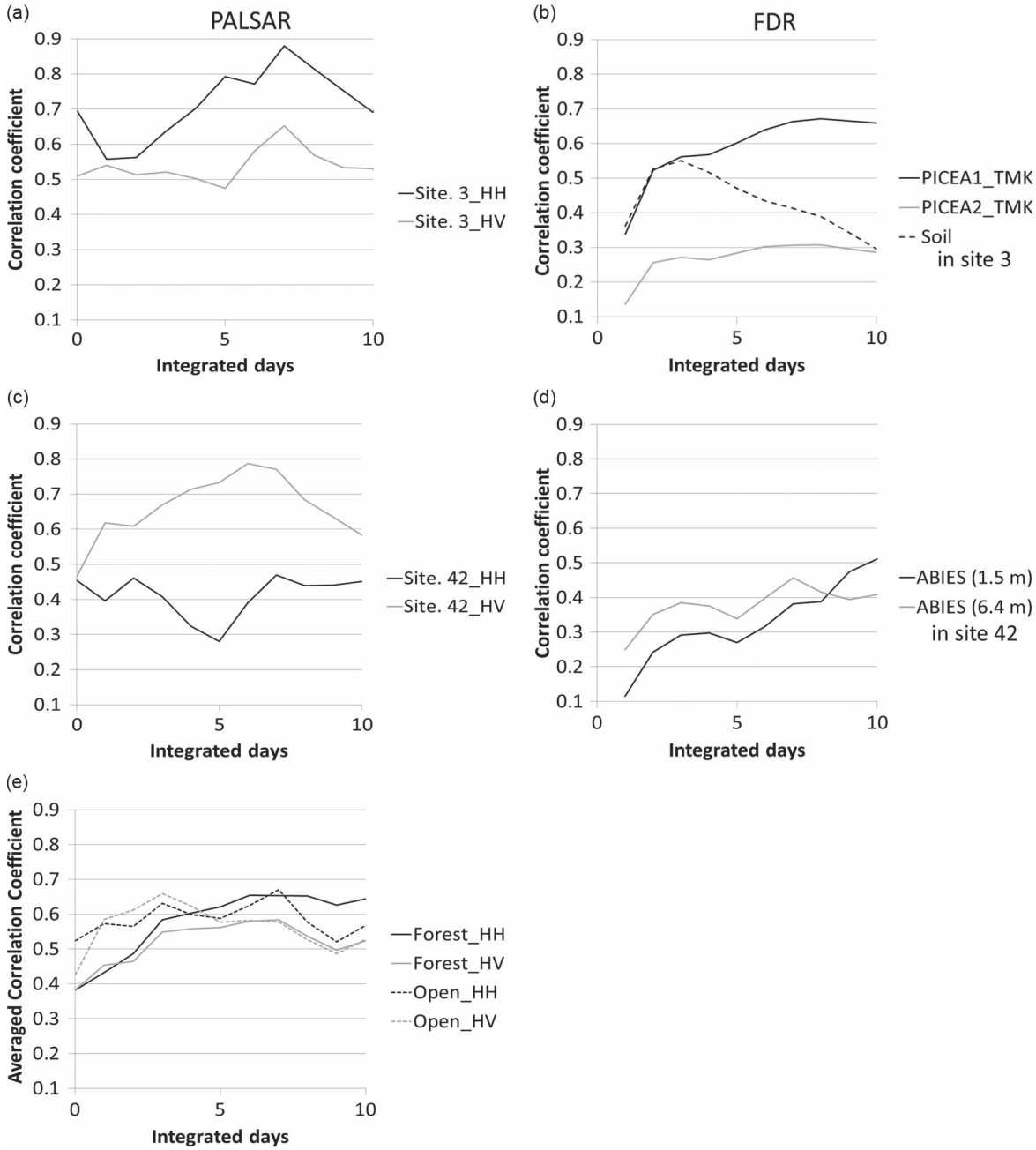

Fig. 8. Dependence of the averaged correlation coefficient r between σ^0 and precipitation on the number of integrated days of precipitation for (a) site 3, (c) site 42, and (e) all sites averaged. Dependence of r between dielectric constant and precipitation for (b) site 3 and (d) site 42.

rainfall of 55 mm was recorded a day before the observation, and the higher soil moisture induces the bright radar backscattering.

D. Correlation Between Temporal Variation of σ^0 and Precipitation

The precipitation data show that there was rainfall for three days before all PALSAR observations, with the exception of October 3, 2007 (see Table II). The averaged σ^0 value, without accounting for the effects of rain, is not available for this data set. The characteristics of the relationships between σ^0 and precipitation are examined for open land and forest areas.

Variations in $\sigma^0_{\text{Open land}}$ can be explained by differences in soil moisture levels. However, variations in σ^0_{Forest} show a slightly different pattern to that of open land. Pearson's correlation coefficient (hereafter r) between σ^0 and the precipitation recorded at the Tomakomai station was calculated.

To determine the number of days, before the PALSAR observation, that should be integrated in order to calculate the amount of precipitation, the relation between r and the number of integrated days was examined for forest and open land and is presented in Fig. 8(e). One integrated day indicates that the precipitation is integrated into the course of one day. In case of a zero integrated day, precipitation during 22:00–23:00 is used since the PALSAR observation was done around 22:30. r gradually increased, reaching the high or highest values for seven integrated days over forest areas. Unlike in forest areas, r

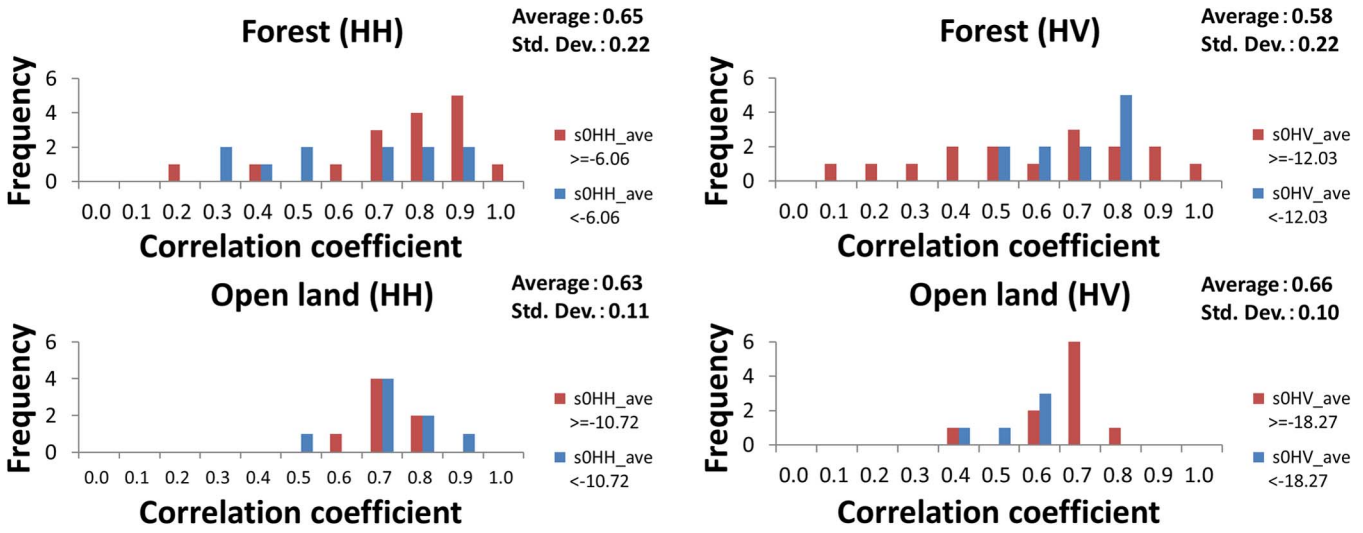

Fig. 9. Histograms of correlation coefficients between σ^0 and precipitation over forest and open areas.

reached a high or highest value for three integrated days over open land. As a result, the precipitation integrated over the seven days before the PALSAR observation was used for forest areas, and three integrated days for open land. During the seven days, precipitation reached a maximum of 71 mm on October 8, 2009 and a minimum of 7 mm on July 11, 2011.

The value of r for σ^0 and precipitation at sites 3 and 42 are presented in Fig. 8(a) and (c), and Fig. 8(b) and (d) shows the r derived from the linear regression analysis between ε and precipitation for a number of integrated days of precipitation at sites 3 and 42. The r value found for $\varepsilon_{\mathrm{Soil}}$ and precipitation [see Fig. 8(b)] shows the highest correlation for three integrated days. The r determined for $\varepsilon_{\mathrm{Tree}}$ and precipitation shows its higher/highest value for eight integrated days. These results are consistent with those derived from PALSAR [see Fig. 8(a)]. The same result is also observed at site 42 [see Fig. 8(c) and (d)].

Fig. 9 shows the histograms of r for σ^0 and precipitation in forest and open land areas. r shows a larger standard deviation of 0.22 for forested areas, and a smaller deviation of 0.1–0.11 for open land. Some forested sites show a higher r of more than 0.7, and the correlation reaches 0.94 in HH polarization and 0.92 in HV polarization. However, some forested sites show a lower r of less than 0.2 for both σ^0_{HH} and σ^0_{HV}. On the other hand, r is distributed around 0.6–0.8 for open land. The dependence of σ^0 was examined and is represented in red/blue in Fig. 9. Red/blue represents the data, where σ^0 is more/less than the average value for the forest/open land. No clear σ^0 dependence is observed, except for σ^0_{HV} for the forest. Forest stands with lower σ^0_{HV}, where less biomass is expected, tend to show a good correlation between σ^0 and precipitation.

The correlation between σ^0_{HV} and the precipitation for eight PICEA areas are shown in Fig. 10. The eight sites contain the same tree species (PICEA), with similar tree ages, planted from 1969 to 1974, except for site 21. ABG measurements were conducted in four of the eight sites, and the values are presented in Fig. 10.

Four sites where strong statistically significant $(\mathrm{P} < 0.01)$ correlations exist are presented in Fig. 10(a)–(d), and four sites where no/weak statistically insignificant $(\mathrm{P} < 0.01)$ correlations exist are presented in Fig. 10(e)–(h). It is confirmed that forest stands with lower σ^0_{HV}, where less biomass is expected, tend to show a strong correlation between σ^0 and precipitation [see Fig. 10(a)–(d)].

Temporal variation of σ^0_{HV} for these areas is plotted in Fig. 11(a), where strong correlation with precipitation was observed, and in Fig. 11(b), where no/weak correlation was observed. When strong correlation exists, all the trajectories of backscatter in the set exhibit the same temporal trend. On the other hand, the four curves presented in Fig. 11(b) are not aligned, whereas the variation pattern is similar. Some areas show strong correlation [see Fig. 10(a)–(d)], some show no/weak correlation [see Fig. 10(e)–(h)], and the others lie in between.

E. Dependence of the σ^0-AGB Relationship to Rainfall

To evaluate how rainfall affects the σ^0-AGB relation, two data sets are selected: one with higher precipitation and the other with lower precipitation. In the higher precipitation data set, three PALSAR data, observed on May 20, 2008 (61.5 mm), July 8, 2009 (55.5 mm), and October 8, 2009 (71 mm), are averaged. In the lower precipitation data set, three PALSAR data, observed on July 5, 2008 (9 mm), October 5, 2008 (9.5 mm), and July 11, 2010 (7 mm), are averaged.

σ^0_{HH}, σ^0_{HV}, and $\sigma^0_{\mathrm{HV}}/\sigma^0_{\mathrm{HH}}$ are plotted against AGB in Fig. 12. An exponential rise-to-maximum model is applied to express these relations, because this functional dependence results in the best fit between L-band HV backscatter and AGB [15]. The equation and fitting results are presented in Fig. 12. For each backscattering coefficient, a 1.9- and 1.8-dB difference is observed. No significant relation is observed in the $\sigma^0_{\mathrm{HV}}/\sigma^0_{\mathrm{HH}}$-AGB plot.

IV. Discussion

A. Temporal Variation of ε and σ^0

Key results from the previous section that will be discussed here are as follows:

1) dependence of dielectric constant (tree and soil) on precipitation;

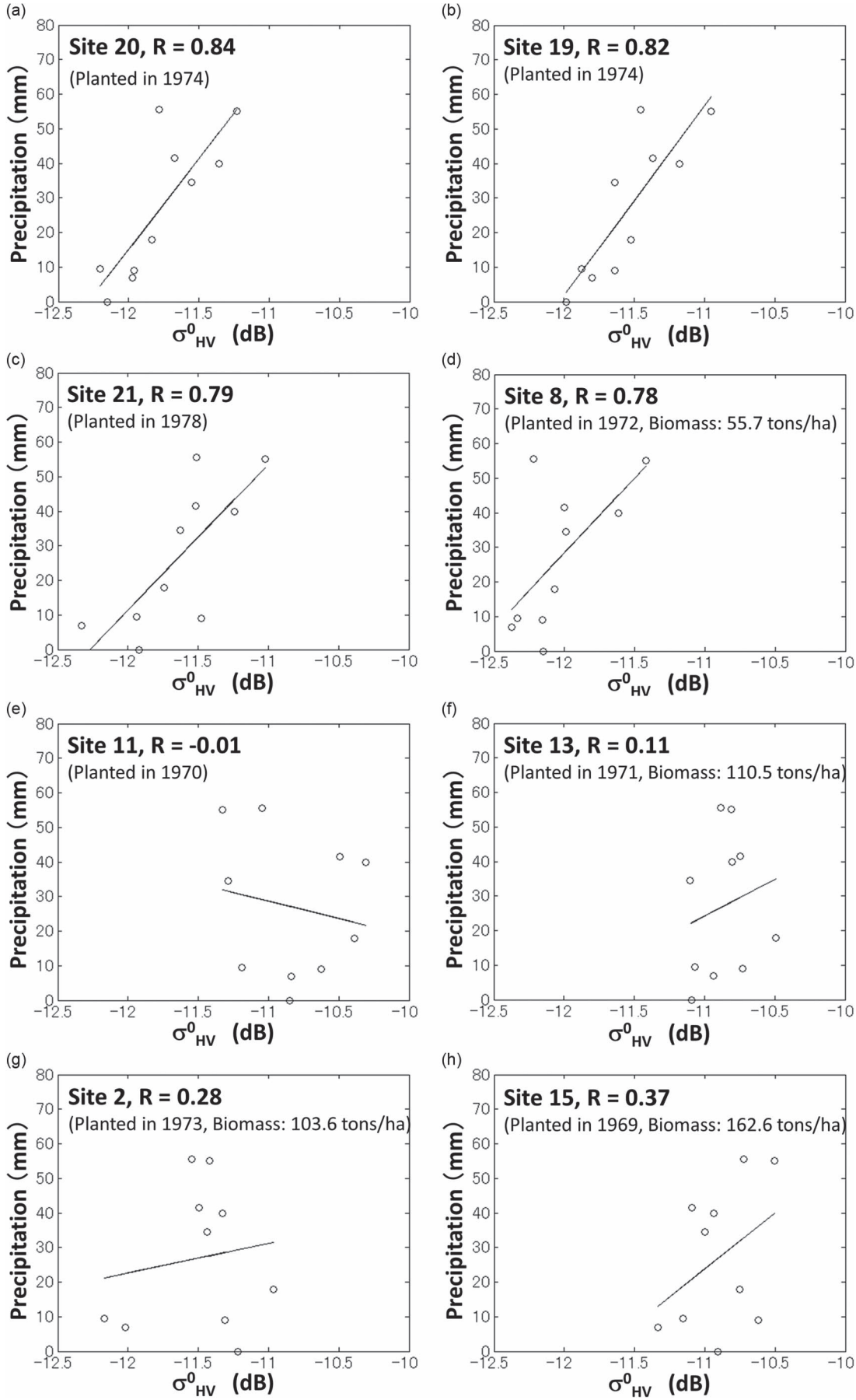

Fig. 10. Correlations between σ^0_{HV} and precipitation. (a)–(d) Four regions where strong correlation exists. (e)–(h) Four regions where weak correlation exists.

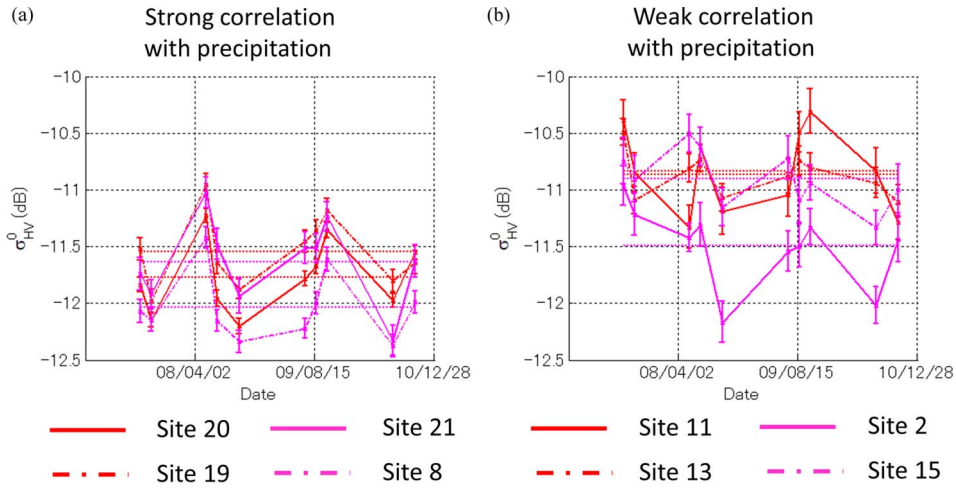

Fig. 11. Temporal variation of σ^0_{HV} over forest area from four regions where (a) strong correlation between σ^0_{HV} and precipitation exists and where (b) weak correlation exists.

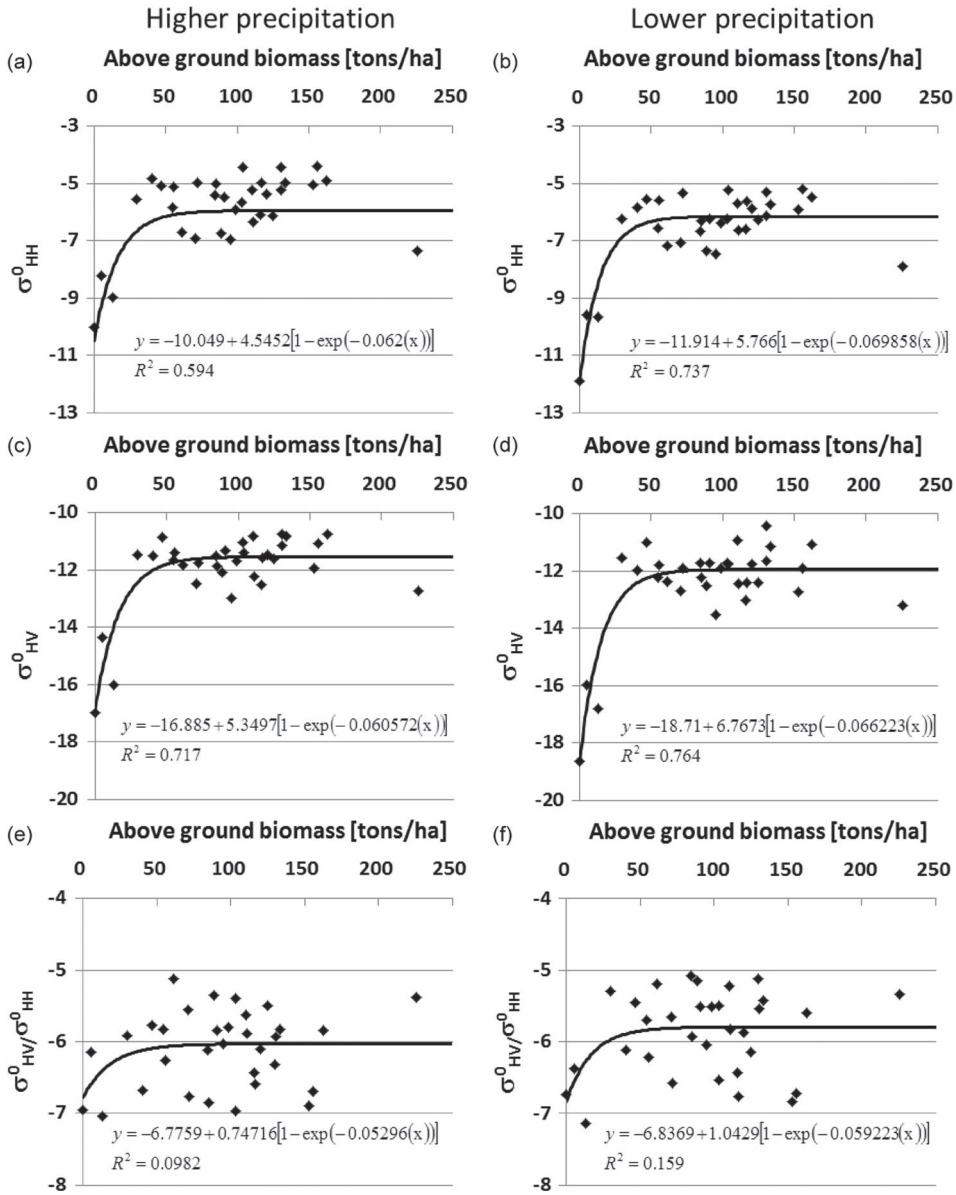

Fig. 12. AGB is plotted against σ^0_{HH} in (a) and (b), σ^0_{HV} in (c) and (d), and $\sigma^0_{\mathrm{HV}}/\sigma^0_{\mathrm{HH}}$ in (e) and (f). Left: PALSAR data sets observed with higher precipitation on three dates are averaged. Right: PALSAR data observed with lower precipitation on three dates are averaged.

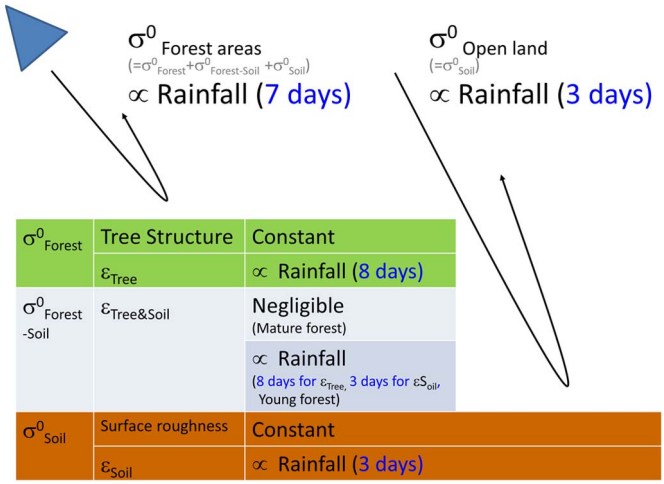

Fig. 13. Sketch of radar reflection from a forest area.

2) how σ^0 varied during the four-year observation (see Section III-C);
3) analysis of possible causes for this variation.

Fig. 13 shows a radar reflection sketch from a forest/open area. $\sigma^0_{\text{Forest area}}$ consists of σ^0_{Forest}, $\sigma^0_{\text{Forest}-\text{Soil}}$, and σ^0_{Soil}. $\sigma^0_{\text{Open area}}$ consists of σ^0_{Soil}. The magnitude of σ^0_{Forest} is dictated by a tree structure and $\varepsilon_{\text{Tree}}$. The tree structure is nearly constant over the course of a few years, whereas $\varepsilon_{\text{Tree}}$ is variable. Measurements indicate that $\varepsilon_{\text{Tree}}$ and σ^0_{Forest} are proportional to precipitation integrated over seven or eight days.

The magnitude of σ^0_{Soil} is dictated by surface roughness and $\varepsilon_{\text{Soil}}$ (or soil moisture). The structure of the surface is nearly constant over the course of a few years, whereas $\varepsilon_{\text{Soil}}$ is variable. Measurements indicate that $\varepsilon_{\text{Soil}}$ and $\sigma^0_{\text{Open land}}$ (or σ^0_{Soil}) are proportional to precipitation integrated over three days.

If the variation in $\sigma^0_{\text{Forest areas}}$ is only dependent on $\varepsilon_{\text{Soil}}$ variation, then $\sigma^0_{\text{Forest areas}}$ should also demonstrate a three-day dependence with precipitation. However, seven-day dependence was observed with precipitation. This fact indicates that $\varepsilon_{\text{Tree}}$ variation contributes to the variation in $\sigma^0_{\text{Forest areas}}$. The integration days indicate the number of days needed to increase the moisture. Soil moisture is directly connected to rainfall, whereas tree moisture is connected not only to rainfall through soil moisture but also to sunshine, air temperature, air moisture content, in addition to other factors [16], [17]. This may cause the difference in integration days between the soil and tree trunk. Strong correlation is observed for $\varepsilon_{\text{Tree}}$ increase$\rightarrow$ advanced rainfall, whereas moderate correlation is observed for advanced rainfall$\rightarrow\varepsilon_{\text{Tree}}$ increase. Waring *et al.* [18] reported some examples of the relationship between sapwood relative water content (Rs) and rainfall. The example shows that Rs increased from 48% to 77% during the six to seven days after rainfall. The other example where more than 300 mm of rain were recorded, Rs only rose by 14%. They concluded that this difference can be explained by potential transpiration, which was estimated from collected field data, and a model and is thought to control sapwood water storage after rain. The moderate correlation observed for advanced rainfall$\rightarrow\varepsilon_{\text{Tree}}$ increase may be explained by this potential transpiration.

TABLE V
FR ESTIMATED FROM PALSAR FULL POLARIMETRY DATA

Observation Date	FR (°)
August 22, 2007	1.95
November 22, 2007	1.95
May 24, 2008	2.40
August 24, 2008	1.48
October 9, 2008	2.08
November 24, 2008	1.34
May 27, 2009	2.07
August 27, 2009	1.52
October 12, 2009	2.23
May 30, 2010	1.93
August 30, 2010	1.96
October 15, 2010	4.10

Strong correlations between σ^0_{HV} and precipitation are observed for both areas with lower σ^0_{HV} and higher σ^0_{HV}. On the other hand, weak correlations are only observed for sites with higher σ^0_{HV}. Less biomass and large $\sigma^0_{\text{Tree trunk}-\text{Soil}}$ contributions are expected to the former, and more biomass and large $\sigma^0_{\text{Forest canopy}}$ are expected to the latter. Simple tree structures with small numbers of scatterers and multiple reflections for the lower biomass area may be one of the possible causes for this stronger correlation. On the other hand, increases of multiple scattering processes caused by longer physical water path (longer trunks/branches) with potential transpiration may often cause lower correlation between σ^0_{HV} and precipitation for the several high biomass areas. By checking σ^0_{Forest} increase with frequent SAR satellite observations, including other frequency (C- and X-band), after rainfall, there is a possibility that information regarding global potential transpiration would be provided.

B. *Effect of the FR*

A linearly polarized wave has its plane of polarization, and the plane rotates as it propagates through the plasma, such as the ionosphere. This is called the Faraday rotation (FR) and causes variations in σ^0. Twelve full polarimetry data observed from 2007 to 2010 in the test site were used to estimate the FR and the variation of the backscatter caused by the FR. The results are presented in Table V. The FR is about 1.9°, except for the data for October 15, 2010, when the FR is 4.1°. This induces a σ^0_{HH} shift of -0.05 dB and a σ^0_{HV} shift of $+0.30$ dB for the data from August 22, 2007 to August 30, 2010 and causes a σ^0_{HH} shift of -0.21 dB and σ^0_{HV} shift of $+1.04$ dB for the data from October 15, 2010. The variation is small for August 22, 2007 to August 30, 2010. Additionally, FR induces opposite phase variation patterns (σ^0_{HH} increase induces σ^0_{HV} decrease).

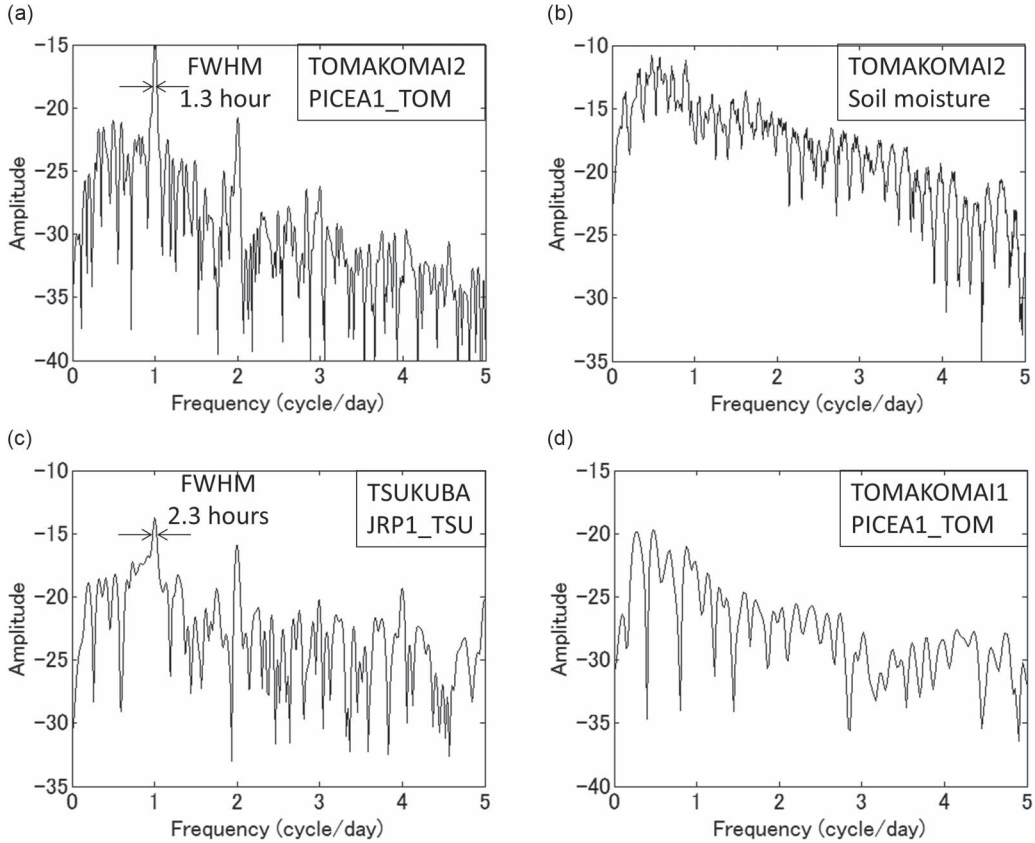

Fig. 14. FFT spectra of time variations of ε shown in Fig. 3.

However, in-phase σ^0 variation (σ^0_{HH} and σ^0_{HV} increase (and decrease) simultaneously) patterns are observed for our data. These facts indicate that observed σ^0 variation is real, and few FR are affected.

C. Diurnal Variation of ε

Fast Fourier transforms (FFTs) were applied to examine the periodicity of the time variation of ε. To remove an offset component and to pick up the periodicity within a 48-h period, a moving window of 48 h is applied for averaging to the time series of ε and was subtracted from the data without averaging. FFT is applied with a Kaiser window for the parameter $\alpha = 32$. The four representative spectra are presented in Fig. 14.

$\varepsilon_{\mathrm{Tree}}$ shows sharp diurnal variations except for the data from PICEA1_TOM of the TOMAKOMAI1 experiment. The full width at half maximum for the peak, around one cycle per day, is 1.3 and 1.1 h for PICEA1_TOM and PICEA2_TOM, respectively, in the TOMAKOMAI2 experiment, and it is 2.3 and 2.0 h for JRP1_TSU and JRP2_TSU, respectively, for the TSUKUBA experiment.

The soil moisture data do not exhibit any diurnal variations in either the Tomakomai [see Fig. 14(b)] or Tsukuba data.

McDonald *et al.* [7], [8] also observed diurnal variation in $\varepsilon_{\mathrm{Tree}}$. For black spruce (or boreal coniferous trees), $\varepsilon_{\mathrm{Tree}}$ maxima occur between 00:00 A.M. and 09:00 A.M., and $\varepsilon_{\mathrm{Tree}}$ minima occur between 12:00 P.M. and 21:00 P.M. On the other hand, balsam poplar (deciduous) trees exhibit their highest $\varepsilon_{\mathrm{Tree}}$ between 12:00 P.M. and 18:00 P.M. Diurnal variation of σ^0 obtained using a P-band ground-based radar deployed above a forest was also reported [19]. As shown in Fig. 3(e), our analysis confirms the results cited in [7] and [19]. The phenomena may be explained by transpiration. During the day, sapwood water content is reduced by the transpiration, whereas at night, the sapwood water content recovers.

D. Qualitative Understanding of $\varepsilon_{\mathrm{Tree}}$ Change

McDonald *et al.* [8] introduced dielectric constant models for free-water and bound-water components to interpret the time-series data, such as dielectric constant, vapor pressure deficit, and xylem sap flux density. The Debye equation is used for the free-water component [20], [21], and it is represented by

$$\varepsilon'_f = \varepsilon_{f\infty} + \frac{\varepsilon_{fs} - \varepsilon_{f\infty}}{1 + \left(\frac{f}{f_{f0}}\right)^2} \tag{2}$$

$$\varepsilon''_f = \frac{\left(\frac{f}{f_{f0}}\right)(\varepsilon_{fs} - \varepsilon_{f\infty})}{1 + \left(\frac{f}{f_{f0}}\right)^2} + \frac{\sigma_{\mathrm{conductivity}}}{2\pi\varepsilon_0 f} \tag{3}$$

where the subscript f denotes free water, and $\varepsilon_{\mathrm{fd}}$ and $\varepsilon_{\mathrm{f}\infty}$ are the static and high-frequency limits of ε'_f; ε_0 is the permittivity of free space, f is the frequency in hertz, f_{f0} is the relaxation frequency, and $\sigma_{\mathrm{conductivity}}$ is the ionic conductivity of aqueous solution in siemens per meter.

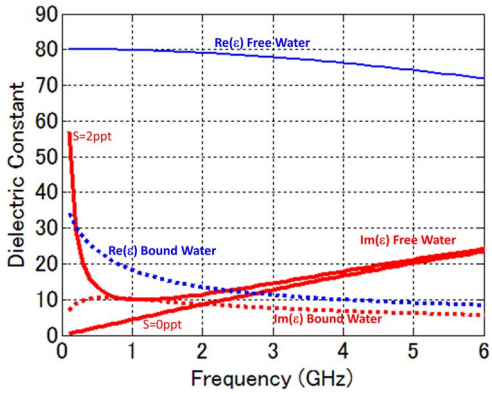

Fig. 15. Dielectric constants (ε) calculated with two models for free water (solid line) and bound water (dashed line), respectively, plotted against frequency. S represents the salinity.

The Cole–Cole dispersion equation was introduced to represent ε with water bound to organic compounds within the vegetation [14], [20], [22], and it is represented by

$$\varepsilon_b = \varepsilon_{\infty b} + \frac{\varepsilon_{0b} - \varepsilon_{\infty b}}{1 + \left(j\frac{f}{f_{0b}}\right)^{1-\alpha_b}} \tag{4}$$

where

$$\varepsilon_{0b} = 35.461 + 0.262T \tag{5}$$

$$\varepsilon_{\infty b} = 6.457 + 0.146T \tag{6}$$

$$\alpha_b = 0.207 + 0.007T \tag{7}$$

$$f_{0b} = 1.296(273 + T)\exp\left(\frac{-1882.238}{273 + T}\right) \tag{8}$$

with T being the temperature in degrees Celsius and f being the frequency in gigahertz. The dielectric constants calculated with these models are plotted against frequency in Fig. 15.

Zero salinity is expected for tree sap, because salt prevents crops from growing. The measured frequency dependence relations of $\varepsilon_{\text{imaginary}}$ (see Fig. 6) were monotonically increasing from 0 to 6 GHz. The measured frequency dependence relations of $\varepsilon_{\text{real}}$ were monotonically decreasing from 0 to 6 GHz. The trends match the theoretical ε for free water and are against the theoretical ε for bound water. This implies that free water is dominant in the measured trees.

McDonald *et al.* [8] pointed out that during periods when $\varepsilon_{\text{Real}}$ and $\varepsilon_{\text{imaginary}}$ are in phase, the composite dielectric constant can be dominated by the free-water product with relatively high ionic conductivity, or it can be dominated by the bound-water product during periods of relatively low ionic conductivity. The former case may be observed in our experiment.

The time lag between $\varepsilon_{\text{Tree}}$ exceeding 1 σ from the seven-day averaged value and the start of rainfall is, on average, 22 h. However, the time lag between the time taken to increase $\varepsilon_{\text{Tree}}$ and the start of rainfall is about 8–9 h after rain began for PICEA1_TOM in the TOMAKOMAI1 experiment. It is 2–3 h after rain began for ABIES_TOM in the complex dielectric constant experiment. The average maximum xylem fluid speed in Norway spruce is typically less than 0.5 m/h with peak values not exceeding 1.2 m/h [23]. Therefore, the time interval may be explained by the time it takes for water to be absorbed by the root.

$\varepsilon_{\text{Tree}}$ and σ^0_{Forest} are proportional to precipitation integrated over seven or eight days, whereas $\varepsilon_{\text{Soil}}$ and $\sigma^0_{\text{Open land}}$ (or σ^0_{Soil}) are proportional to precipitation integrated over three days. The longer period of integrated days may also be explained by the traveling time of the xylem sap to the tree canopy.

E. Rainfall Contribution to the AGB/σ^0 Relation

The relation between AGB and σ^0 shows dependence on rainfall. The coefficient of determination (R^2) for the lower precipitation data set is a better fit than that of the higher precipitation data set in σ^0_{HH}. This is mainly because σ^0 for the three stands with the lowest biomass is increased by rain, as shown in Fig. 12. Rainfall often induces a disturbance in $\varepsilon_{\text{Tree}}$ and may negatively affect the relation between AGB and σ^0. Lucas *et al.* [3] also demonstrated that σ^0-AGB depended on surface moisture (including the tree canopy and soil), estimated from AMSR-E data, and showed a better correlation under minimal rainfall conditions. The results of this study support those results and reinforce the fact that the dry season is preferable for retrieval of woody biomass from inversion of the functional dependence of SAR backscatter and for avoiding the influence of rainfall.

V. Summary and Conclusion

Temporal variations (diurnal and annual) in arboreal $(\varepsilon_{\text{Tree}})$ and bare soil $(\varepsilon_{\text{Soil}})$ dielectric constants and their correlations with precipitation data were examined for trees in Japan. Significant (1 and 2 σ) $\varepsilon_{\text{Tree}}$ increase is induced by rainfall with 89.8% and 90.5% probability. On the other hand, rainfall of more than 5 mm/day induces a 1 σ $\varepsilon_{\text{Tree}}$ increase with a 59.6% probability. Moderate correlation observed for advanced rainfall$\rightarrow\varepsilon_{\text{Tree}}$ increase may be explained by an additional parameter, i.e., potential transpiration, which controls sapwood water storage after rain [18].

To examine if $\varepsilon_{\text{Tree}}$ increase affects L-band σ^0 variation in a forest, the temporal variations of σ^0 in the Tomakomai National Forest are examined using four years of PALSAR data. Maximum deviations from the mean of 1.0 and 1.2 dB are observed in HH and HV polarizations, respectively, in forested areas, and maximum deviations from the mean of 4.0 and 3.0 dB over open land.

The main results were as follows.

1) For forest areas, consistent functional dependence was found between both σ^0 and ε and precipitation integrated over seven or eight days, whereas for open land, a relationship was found with precipitation integrated over three days (see Fig. 8). This fact indicates that $\varepsilon_{\text{Tree}}$ variation contributes to the variation in $\sigma^0_{\text{Forest areas}}$.
2) The correlation analysis of σ^0 and precipitation did not yield consistent results (with coefficients varying from 0.2 to 0.9; see Fig. 9). Strong correlations between σ^0_{HV} and precipitation are observed for both areas with lower σ^0_{HV} and higher σ^0_{HV}. Weak correlations are only observed for

sites with higher σ^0_{HV}. Increases of the multiple scattering processes caused by longer water path (longer trunk and branch) with different potential transpiration conditions may induce the lower correlation between σ^0_{HV} and precipitation for the several high biomass areas.

3) The functional relation between AGB and σ^0 showed dependence on precipitation data. The coefficient of determination for the lower precipitation data set shows a better fit than that of the higher precipitation data set for σ^0_{HH} (see Fig. 12). The results reinforce the fact that the dry season is preferable for the retrieval of woody biomass from L-band σ^0.
4) The complex dielectric constant of a tree trunk, measured between 0.2 and 6 GHz, indicates that free water is dominant in the measured tree (see Fig. 6).

This experiment indicates that the dry season is preferable for retrieval of woody biomass from inversion of the functional dependence of SAR backscatter and for avoiding the influence of rainfall.

ACKNOWLEDGMENT

The authors would like to thank Prof. K. Ouchi and his student (National Defense Academy) for assisting with the field activities, Dr. T. Hirano (Hokkaido University) for providing the precipitation data for the Tomakomai National Forest, Dr. N. Saegusa (National Institute for Environmental Studies), Dr. K. Nishida Nasahara (Tsukuba University), S. Iida (Forestry and Forest Products Research Institute), and T. Kumagai (Nagoya University) for providing guidance on plant physiology.

REFERENCES

[1] M. C. Dobson *et al.*, "Dependence of radar backscatter on coniferous forest biomass," *IEEE Trans. Geosci. Remote Sens.*, vol. 30, no. 2, pp. 412–415, Mar. 1992.
[2] M. Watanabe *et al.*, "Forest structure dependency of the relation between L-band σ^0 and biophysical parameters," *IEEE Trans. Geosci. Remote Sens.*, vol. 44, no. 11, pp. 3154–3165, Nov. 2006.
[3] R. Lucas *et al.*, "An evaluation of the ALOS PALSAR L-band backscatter—Above ground biomass relationship Queensland, Australia: Impacts of surface moisture condition and vegetation structure," *IEEE J. Sel. Topics Appl. Earth Observ. Remote Sens.*, vol. 3, no. 4, pp. 576–593, Dec. 2010.
[4] S. C. Steele-Dunne, J. Friesen, and N. de Giesen, "Using diurnal variation in backscatter to detect vegetation water stress," *IEEE Trans. Geosci. Remote Sens.*, vol. 50, no. 7, pp. 2618–2629, Jul. 2012
[5] Y. Rauste, "Multi-temporal JERS SAR data in boreal forest biomass mapping," *Remote Sens. Environ.*, vol. 97, no. 2, pp. 263–275, Jul. 2005
[6] J. Way *et al.*, "Evaluating the type and state of Alaska taiga forests with imaging radar for use in ecosystem models," *IEEE Trans. Geosci. Remote Sens.*, vol. 32, no. 2, pp. 353–370, Mar. 1994.
[7] K. C. McDonald, R. Zimmermann, J. B. Way, and W. Chun, "Automated instrumentation for continuous monitoring of the dielectric properties of woody vegetation: System design, implementation, and selected in situ measurements," *IEEE Trans. Geosci. Remote Sens.*, vol. 37, no. 4, pp. 1880–1894, Jul. 1999.
[8] K. C. McDonald, R. Zimmermann, and J. S. Kimball, "Diurnal and spatial variation of xylem dielectric constant in Norway spruce (Picea abies [L.] Karst.) as related to microclimate, xylem sap flow, and xylem chemistry," *IEEE Trans. Geosci. Remote Sens.*, vol. 40, no. 9, pp. 2063–2082, Sep. 2002.
[9] W. A. Salas, J. K. Ranson, B. N. Rock, and K. T. Smith, "Temporal and spatial variations in dielectric constant and water status of dominant forest species from New England," *Remote Sens. Environ.*, vol. 4, no. 2, pp. 109–119, 1994.
[10] Project Department, Forestry Agency Ed., Stand Volume Table-East Japan, Japan Forestry Investigation Committee, Tokyo, Japan, Oct. 1998.
[11] Wood Industrial Handbook, Forestry and Forest Products Research Institute, Ed., Maruzen, Tsukuba, Japan, 1982.
[12] E. Pottier *et al.*, "Overview of the PolSARpro V4.0 software. The open source toolbox for polarimetric and interferometric polarimetric SAR data processing," in *Proc. IEEE Geosci. Remote Sens. Symp.*, 2009, vol. 4, pp. 936–939.
[13] M. Shimada, O. Isoguchi, T. Tadono, and K. Isono, "PALSAR radiometric and geometric calibration," *IEEE Trans. Geosci. Remote Sens.*, vol. 47, no. 12, pp. 3915–3932, Dec. 2009.
[14] M. A. El-rayes and F. T. Ulaby, "Microwave dielectric spectrum of vegetation—Part I: Experimental Observations," *IEEE Trans. Geosci. Remote Sens.*, vol. GE-25, no. 5, pp. 541–549, Sep. 1987.
[15] E. T. A. Mitchard *et al.*, "Measuring biomass changes due to woody encroachment and deforestation/degradation in a forest–savanna boundary region of central Africa using multi-temporal L-band radar backscattering," *Remote Sens. Environ.*, vol. 115, no. 11, pp. 2861–2873, Nov. 2011.
[16] D. M. Gates, "Water relations of forest trees," *IEEE Trans. Geosci. Remote Sens.*, vol. 29, no. 6, pp. 836–842, Nov. 1991.
[17] M. Williams *et al.*, "Modelling the soil–plant–atmosphere continuum in a Quercus-Acer stand at Harvard Forest: The regulation of stomatal conductance by light, nitrogen and soil/plant hydraulic properties," *Plant Cell Environ.*, vol. 19, no. 8, pp. 911–927, Aug. 1996
[18] R. H. Waring and S. W. Running, "Sapwood water storage: Its contribution to transpiration and effect upon water conductance through the stems of old-growth Douglas-fir Plant," *Cell Environ.*, vol. 1, no. 2, pp. 131–140, Jun. 1978.
[19] A. Hamadi *et al.*, "Temporal survey of polarimetric P-band scattering of tropical forests," *IEEE Trans. Geosci. Remote Sens.*, vol. 52, no. 8, pp. 4539–4547, Aug. 2014.
[20] F. T. Ulaby and M. A. El-Rayes, "Microwave dielectric spectrum of vegetation—Part II: Dual-dispersion model," *IEEE Trans. Geosci. Remote Sens.*, vol. GE-25, no. 5, pp. 550–557, Sep. 1987.
[21] F. T. Ulaby, R. K. Moore, and A. K. Fung, *Microwave Remote Sensing: Active and Passive*, vol. 3. Dedham, MA, USA: Artech House, 1986, pp. 2022–2025.
[22] M. A. El-Rayes and F. T. Ulaby, "Microwave dielectric behavior of vegetation material," Dept. Elect. Eng. Comput. Sci., Univ. Michigan, Ann Arbor, MI, USA, Radiation Lab. Tech. Rep. RL-022 132 030T, Jan. 1987.
[23] W. Larcher, *Physiological Plant Ecology*. Berlin, Germany: Springer-Verlag, 1975, p. 252.

Manabu Watanabe (SM'14) received the B.Sc. degree in physics from Shinsyu University, Nagano, Japan, in 1991 and the Ph.D. degree in astrophysics (using Japanese X-ray astronomy satellite data) from Nagoya University, Nagoya, Japan, in 2000.

He was a Researcher with the Japan Aerospace Exploration Agency (JAXA), where he was a part of the Daichi (ALOS) data analysis group. At Tohoku University, Miyagi, Japan, between 2007 and 2011, he developed a ground-based scatterometor system and examined the radar reflection from permafrost. He is currently with JAXA, analyzing SAR data for understanding radar scattering from forests and disaster areas. He has authored or coauthored several conference papers.

Dr. Watanabe is a member of the Remote Sensing Society of Japan.

Takeshi Motohka received the Ph.D. degree in environmental sciences from the University of Tsukuba, Tsukuba, Japan, in 2009.

From 2009 to 2010, he was a Postdoctoral Research Fellow with the Japan Society for the Promotion Science. He is currently a Researcher with the Japan Aerospace Exploration Agency, Tsukuba, and is a member of the ALOS and ALOS-2 science team. His research interests include developing algorithms and products for terrestrial ecosystem monitoring using various remote sensing sensors such as SAR, optical imager, and LiDAR.

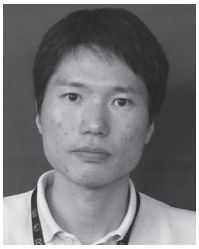

Tomohiro Shiraishi received the Bachelor's and Master's degrees in system electronic engineering from the Tokyo University of Technology, Tokyo, Japan, in 1998 and 2000, respectively.

From 2000 to 2007, he worked with software development companies. He was a Researcher with the Fukuoka Industry, Science and Technology Foundation, Fukuoka, Japan, from 2007 to 2010 and with the Japan Aerospace Exploration Agency, Tsukuba, Japan, from 2010 to 2013. His research interests include software engineering, formal verification, machine learning, and SAR data analysis.

Rajesh Bahadur Thapa received the M.A. degree in geography from Tribhuvan University (TU), Kathmandu, Nepal, in 1998; the M.Sc. degree in Remote Sensing and Geographic Information Systems from the Asian Institute of Technology (AIT), Khlong Luang, Thailand, in 2003; and the Ph.D. degree in geoenvironmental science from the University of Tsukuba (UT), Tsukuba, Japan, in 2009.

He was a Lecturer with TU from 1998 to 2002, a Researcher with the AIT from 2004 to 2005, and a Japan Society for the Promotion of Science Postdoctoral Fellow with UT from 2009 to 2011. Since 2011, he has been an Invited Researcher with the Earth Observation Research Center, Japan Aerospace Exploration Agency, Tsukuba. He is the author of two books and a contributor of many articles in peer-reviewed journals. His research interests include retrieval of forest biomass from radar backscatters, land-use–land-cover classification, land change analysis, and spatial modeling.

Dr. Thapa was a recipient of the University of Tsukuba Outstanding Research Award in 2008 and the Nepal Biddya Bhusan First Class Award for academic achievement from the President of Nepal in 2010.

Chinatsu Yonezawa (M'00) received the Ph.D. degree in earth and planetary sciences from the University of Tokyo, Tokyo, Japan, in 2002.

She was a Research Scientist with the Remote Sensing Technology Center of Japan, Tokyo, from 1996 to 2005 and a Lecturer with Miyagi University, Miyagi, Japan, from 2005 to 2009. She is currently an Associate Professor with the Graduate School of Agricultural Science, Tohoku University, Miyagi, Japan. Her main research interest is the application of remote sensing, including SAR observation in agricultural science.

Kazuki Nakamura (M'04) was born in Tokyo, Japan, in 1974. He received the B.E. degree in integrated arts and sciences and the M.E. degree in education from Hokkaido University of Education, Hokkaido, Japan, in 1998 and 2000, respectively, and the Ph.D. degree in science from Chiba University, Chiba, Japan, in 2003.

He was a Postdoctoral Fellow in remote sensing science with the Communications Research Laboratory (currently the National Institute of Information and Communications Technology), Koganei, Tokyo, from 2003 to 2006 and with the National Institute for Polar Research, Itabashi, Tokyo (currently Tachikawa, Tokyo), from 2006 to 2007. During 2007–2012, he was a Postdoctoral Fellow in remote sensing science with the National Institute of Advanced Industrial Science and Technology, Tsukuba, Ibaraki, Japan. Since 2012, he has been an Associate Professor with the Department of Computer Science, College of Engineering, Nihon University, Koriyama, Fukushima, Japan. His research interest is in microwave remote sensing of sea ice, glacier, and various targets of the earth.

Masanobu Shimada (M'97–SM'04–F'11) received the B.S. and M.S. degrees in aeronautical engineering from Kyoto University, Kyoto, Japan, in 1977 and 1979, respectively, and the Ph.D. degree in electrical engineering from the University of Tokyo, Tokyo, Japan, in 1999.

In 1979, he joined the National Space Development Agency of Japan [NASDA; formerly the Japan Aerospace Exploration Agency (JAXA)], where he designed the NASDA scatterometer by 1985. From 1985 to 1995, he developed data processing systems for optical and SAR data (MOS-1, SPOT, and JERS-1) at the Earth Observation Center. He was a one-year Visiting Scientist at the Jet Propulsion Laboratory in 1990. After launch of JERS-1 in 1992, he was in charge of the JERS-1 SAR calibration and validation. Since 1995, he has been assigned duties at the Earth Observation Research Center, where he is in charge of the JERS-1 Science project (global rainforest and boreal forest mapping project and SAR interferometry project). He also developed a polarimetric airborne SAR (Pi-SAR-L) and calibrated the Ocean Color Temperature Scanner and AVNIR of ADEOS. In the late 1990s, he initiated the ALOS science project, which has calibration and validation of the ALOS sensors. He mainly focuses on PALSAR calibration, validation, and application. He also initiated the Kyoto and Carbon Initiative project for monitoring the forest and wetland using the time-series PALSAR mosaics. His main outputs are the global SAR mosaics showing the annual deforestation change and large-scale land surface deformations. He has been a Principal Researcher with JAXA and leading the ALOS and ALOS-2 science projects. His current research interests are high-resolution imaging for spaceborne and airborne SARs (PALSAR-2 and Pi-SAR-L2), calibration and validation, and SAR applications including polarimetric SAR interferometry.